High-precision 3D Location and Orientation Tracking using Multi-Sensor Cellular Carrier Phase Measurements

Antti Saikko, Jukka Talvitie, and Mikko Valkama
Department of Electrical Engineering, Tampere University, Tampere, Finland

***Abstract*—Recent 5G-Advanced cellular specifications introduce several positioning enhancements, including carrier phase measurements that enable high-precision 3D localization at the accuracy scale of used radio frequency (RF) wavelength. Besides localization, in numerous use cases from extended reality (XR) headsets to industrial automation and heavy machines, accurate knowledge of the device 3D orientation is of paramount importance together with low latency operation. In this paper, utilizing multi-sensor carrier phase measurements, we address high-precision joint tracking of device 3D location and orientation, where the full device state can be directly estimated at the network side, thus enabling very low latency and response times for possible device-related network actions. The proposed tracking approach builds on extended Kalman filter framework, and is supplemented with a particle filter solution which handles the challenging integer ambiguity problem and maintains synchronization between the network and device under clock drifting. Furthermore, multi-frequency carrier phase measurements through carrier-aggregation are addressed to further improve the performance. Based on numerical evaluations, we show that the proposed 3D location and orientation tracking achieves sub-centimeter and sub-degree accuracy for position and orientation estimation, respectively, while also enabling sub-nanosecond network synchronization.**

***Index Terms*—3D orientation estimation, 3D positioning, 5G-Advanced, 6G, tracking, carrier phase, integer ambiguity**

I. Introduction

The advent of 5G-Advanced and beyond cellular technologies has launched a new era of high-precision positioning technologies, essential for a myriad of applications ranging from industrial automation to Vehicle-to-everything (V2X) and extended reality (XR) [1], [2]. Among these technologies, cellular Carrier Phase Positioning (CPP) stands out due to its potential to achieve sub-centimeter-level positioning accuracy [1], [3]. In addition to tracking of 3D position of the device, tracking 3D orientation while overcoming low latency requirements is of great importance to many use cases from industrial automation to XR and immersive holographic-type communications [4], [5].

Along with developments in 3rd Generation Partnership Project (3GPP) standardization, research on cellular CPP has attained growing attention in the literature [3], [6]–[9]. In [3], theoretical bounds on CPP have been derived based on mixed integer programming to properly address the challenging integer ambiguity problem. In [6] and [7], CPP has been investigated in indoor and Industrial Internet-of-Things (IIoT) scenarios, respectively, while [8], [9] focus on CPP with multi-carrier measurements.

This work was supported by the Research Council of Finland (grant 359095) and by Business Finland under the AURORA project.

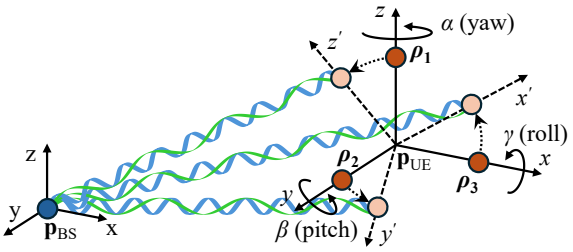

Fig. 1. Illustration of the basic concept considering multi-frequency measurements with a single BS, and a UE equipped with multiple antennas.

In this paper, we address high-precision and low-latency 3D location and orientation tracking of user equipment (UE), equipped with multiple antennas, while using multi-frequency carrier phase measurements. Through utilization of uplink measurements, the proposed tracking approach enables close to real time 3D orientation estimation at the network side, which is not generally reachable by conventional UE-based methods utilizing, for example, inertial sensors or Angle-of-Arrival measurements, due to additional measurement reporting delays. Compared to our earlier work in [5], the proposed extended Kalman filter (EKF) based tracking approach introduces a specific cycle control mechanism and utilization of multi-frequency measurements for handling integer ambiguity problem in high mobility scenarios. Additionally, to further push the limits of tracking performance, we formulate a particle filter solution on top of the EKF framework, which shows superior tracking performance for large measurement intervals or high UE mobility.

The main contributions of this paper are given as follows:

- We formulate multi-sensor and multi-frequency EKF-based tracking for user 3D localization and 3D orientation estimation using carrier phase measurements;
- We propose a specific consecutive EKF measurement update processing, which increases tolerance against integer ambiguity issues in high mobility scenarios;
- We formulate a particle filter solution to extend the tracking capability to even higher mobility scenarios;
- We assess the performance of proposed methods in a dynamic scenario with varying 3D location and 3D orientation of the UE along with a drifting UE clock.

The rest of the paper is organized as follows: Section II describes the system model for carrier phase measurements and Section III introduces the proposed tracking methods, including EKF and particle filter solutions. Finally, Section IV presents

the numerical evaluations, and Section V concludes the paper.

II. System Model

In this section, we describe the considered 3D localization and orientation tracking concept, and define the measurement model for the considered carrier phase measurements.

A. General Concept and Unknown UE State Vector

We consider a system with a moving and rotating UE and M stationary base stations (BSs) or other network transmission/reception points (or even distributed antenna points) with known locations and orientations. In Fig. 1, the considered system is illustrated for a single BS and UE located at $\mathbf{p}_{\text{BS}}$ and $\mathbf{p}_{\text{UE}}$, respectively. The UE is equipped with N antennas at positions $\boldsymbol{\rho}_n$, defined relative to the UE position in the BS reference coordinate frame (x,y,z) for $n = 1, \ldots, N$. Assuming $\mathbf{p}_{\text{UE}}$ as the center point of rotation, the 3D UE orientation can be altered through rotations of z-axis, y-axis and x-axis, which describe the device yaw α, pitch β and roll γ, respectively.

The considered system can be applied to both downlink and uplink scenarios and incorporate carrier phase measurements from Q frequency bands. Furthermore, BSs are assumed mutually synchronized, while the UE clock is unsynchronized and drifting in time. At time instant k, the time-varying UE clock δ_k is defined as [10]

$$\begin{aligned} \delta_k &= \delta_{k-1} + \Delta\delta_k \Delta t \\ \Delta\delta_k &= \Delta\delta_{k-1} + \xi_k, \end{aligned} \tag{1}$$

where Δt denotes the measurement interval between two consecutive time instants, and $\Delta\delta_k$ is a time-varying clock skew with $\xi_k \sim \mathcal{N}(0, \sigma_\xi^2)$.

The unknown state vector at time step k, incorporating the six degrees-of-freedom (6DoF) state parameters and a drifting clock of the UE, is determined as

$$\mathbf{s}_k = \begin{bmatrix} \boldsymbol{\theta}_k^T & \boldsymbol{\Delta\theta}_k^T & \mathbf{p}_{\text{UE},k}^T & \mathbf{v}_{\text{UE},k}^T & \delta_k & \Delta\delta_k \end{bmatrix}^T \in \mathbb{R}^{14} \tag{2}$$

where $\boldsymbol{\theta}_k = [\alpha_k, \beta_k, \gamma_k]^T$ describes the 3D UE orientation, and $\mathbf{p}_{\text{UE},k} = [x_{\text{UE},k}, y_{\text{UE},k}, z_{\text{UE},k}]^T$ is the UE position with the x, y and z coordinate. Furthermore, UE motion is represented with the rotational rate-of-change $\boldsymbol{\Delta\theta}_k = [\Delta\alpha_k, \Delta\beta_k, \Delta\gamma_k]^T$, including distinct rates-of-change of rotation angles α, β and γ, respectively, and the UE velocity $\mathbf{v}_{\text{UE},k} = [v_{\text{x},k}, v_{\text{y},k}, v_{\text{z},k}]^T$, defined relative to the x-axis, y-axis and z-axis, respectively.

B. Measurement Model

The considered system utilizes antenna-level carrier phase measurements between the N UE antennas and M BS antennas. For the k^{th} time step and q^{th} frequency band, the carrier phase-based range measurements between the n^{th} UE antenna and m^{th} BS can be written as

$$\phi_{n,m,k}^q = h_{n,m}^q(\mathbf{s}_k) + n_{n,m,k}^q, \tag{3}$$

where $h_{n,m}^q \colon \mathbb{R}^{14} \to \mathbb{R}$ is the measurement function, and $n_{n,m,k}^q \sim \mathcal{N}(0, \sigma)$ denotes measurement noise with variance σ. Moreover, let us assume a signal wavelength of $\lambda_q = c/f_q$, where c and f_q are the speed of light and carrier frequency of the q^{th} frequency band, respectively. Then, the measurement function, describing an ambiguous range measurement, can be expressed as [11]

$$h_{n,m}^q(\mathbf{s}_k) = \|\mathbf{p}_{\text{UE},k} + \mathbf{R}(\boldsymbol{\theta}_k)\boldsymbol{\rho}_n - \mathbf{p}_{\text{BS},m}\| + c\delta_k - Z_{n,m,k}^q \lambda_q, \tag{4}$$

where the norm term and $Z_{n,m}^q \in \mathbb{Z}$ indicate the range and integer ambiguity between the n^{th} UE antenna element and m^{th} BS. In addition, the term $c\delta_k$ represents the ranging bias due to UE clock error, and $\mathbf{R}(\boldsymbol{\theta}) \in \mathbb{R}^{3\times3}$ is the 3D rotation matrix [12] realizing the UE orientation. It is noted that in practice carrier phase measurements are indeed phase measurements, however, the range measurements in (3) and (4) can be easily expressed in radians as $2\pi\phi_{n,m,k}^q/\lambda_q$.

Considering sequential measurements over time index k, it is possible to obtain unwrapped carrier phase measurement

$$\Phi_{n,m,k}^q = Z_{m,n,1}^q \lambda_q + \mathfrak{U}(\phi_{n,m,k}^q) + \Psi_{m,n,k}^q \lambda_q \tag{5}$$

where $Z_{m,n,1}^q$ is the integer ambiguity at first time step $k = 1$. Furthermore, $\mathfrak{U}(\phi_{n,m,k}^q) = \phi_{n,m,k}^q + \Psi_{m,n,k}^q \lambda_q$ is an unwrapping function where $\Psi_{m,n,k}^q \in \mathbb{Z}$ is chosen so that the difference between consecutive fractional range measurements is within the half-wavelength ($|\phi_{n,m,k-1}^q - \phi_{n,m,k}^q| < \lambda_q/2$). The unwrapped measurements can be seen as cumulative range measurements subject to clock bias.

III. Proposed Methods

In this section, we present the proposed EKF-based tracking formulation with specific cycle control mechanism and utilization of multi-frequency measurements. Furthermore, we describe a particle filter-based solution to improve tolerance against cycle slips in high mobility scenarios.

A. State-Transition Model and State Prediction

We assume that the UE velocity, rotational rate-of-change and clock drift are near constant over a short time period. Consequently, we employ a linear constant white-noise acceleration (CWNA) mobility model [13] and express a state-transition between time steps $k-1$ and k as

$$\mathbf{s}_k = \mathbf{F}\mathbf{s}_{k-1} + \mathbf{w}_k \tag{6}$$

where $\mathbf{F} \in \mathbb{R}^{14\times14}$ is the state-transition matrix, and $\mathbf{w}_k \sim \mathcal{N}(0, \mathbf{Q}) \in \mathbb{R}^{14}$ is the process noise. Furthermore, the state-transition matrix is expressed as

$$\mathbf{F} = \text{blkdiag}(\boldsymbol{\mathcal{F}} \otimes \mathbf{I}_3, \boldsymbol{\mathcal{F}} \otimes \mathbf{I}_3, \boldsymbol{\mathcal{F}}), \text{ where } \boldsymbol{\mathcal{F}} = \begin{bmatrix} 1 & \Delta t \\ 0 & 1 \end{bmatrix}, \tag{7}$$

where $\otimes$ denotes the Kronecker product and $\text{blkdiag}(\mathbf{A}_1, \mathbf{A}_2, \mathbf{A}_3)$ refers to a block diagonal matrix constructed from matrices $\mathbf{A}_1$, $\mathbf{A}_2$, and $\mathbf{A}_3$ in respective order. By following the CWNA model in [13], the process covariance matrix $\mathbf{Q} \in \mathbb{R}^{14\times14}$ is defined as

$$\begin{aligned} \mathbf{Q} &= \text{blkdiag}(\sigma_{\Delta\theta}^2 \boldsymbol{\mathcal{Q}} \otimes \mathbf{I}_3, \sigma_{\text{v}}^2 \boldsymbol{\mathcal{Q}} \otimes \mathbf{I}_3, \sigma_{\Delta\delta}^2 \boldsymbol{\mathcal{Q}}) \in \mathbb{R}^{14\times14}, \\ &\text{where } \boldsymbol{\mathcal{Q}} = \begin{bmatrix} \frac{\Delta t^3}{3} & \frac{\Delta t^2}{2} \\ \frac{\Delta t^2}{2} & \Delta t \end{bmatrix}. \end{aligned} \tag{8}$$

The magnitude of process covariance is assessed through parameters $\sigma^2_{\Delta\theta}$, σ^2_{v} and $\sigma^2_{\Delta\delta}$, which describe the power spectral density of angular acceleration of rotation angles (α, β and γ), UE acceleration with respect to component axes (x_{UE}, y_{UE}, z_{UE}), and acceleration of clock error, respectively. Finally, given the state-transition model in (6), the prediction step of the EKF at time index k is expressed as

$$\begin{aligned}\hat{\mathbf{s}}_k^- &= \mathbf{F}\hat{\mathbf{s}}_{k-1}^+ \\ \hat{\mathbf{P}}_k^- &= \mathbf{F}\hat{\mathbf{P}}_{k-1}^+\mathbf{F}^T + \mathbf{Q}\end{aligned} \tag{9}$$

where $\hat{\mathbf{s}}_k^- \in \mathbb{R}^{14}$ and $\hat{\mathbf{P}}_k^- \in \mathbb{R}^{14\times 14}$ are the a-priori estimates of the mean and covariance of the UE state, respectively. Furthermore, $\hat{\mathbf{s}}_{k-1}^+$ and $\hat{\mathbf{P}}_{k-1}^+$ denote the mean and covariance for the a-posteriori state estimate of the previous time step $k-1$.

B. Addressing Varying Integer Ambiguity via Cycle Control

UE motion induces a varying integer ambiguity, which could be tracked as part of the UE state [5]. However, considering the unwrapped measurements in (5), if the ambiguous range measurement $\phi^q_{n,m,k}$ does not change more than half-wavelength between consecutive time steps ($\forall(k,n,m)\, \Psi^q_{m,n,k} = 0$), the unwrapped measurements provide effectively an unambiguous range measurements. However, with high UE state dynamics, the change in range measurements between consecutive time steps can cover multiple wavelengths ($\exists(k,n,m)\, \Psi^q_{m,n,k} \neq 0$) which is not captured by the unwrapping function $\mathfrak{U}(\phi^q_{n,m,k})$.

Considering the availability of a predicted UE state $\hat{\mathbf{s}}_k^-$, possible cycle jumps over multiple wavelengths with unwrapped measurements can be recursively approximated as

$$\hat{\Psi}^q_{m,n,k} = \begin{cases} \hat{\Psi}^q_{m,n,k-1}, & |\varepsilon^q_{n,m}| < \lambda_q/2, \\ \hat{\Psi}^q_{m,n,k-1} + \mathcal{R}(\varepsilon^q_{n,m}/\lambda_q), & \text{otherwise}, \end{cases} \tag{10}$$

where for the first time index $\hat{\Psi}^q_{m,n,1} = 0$. Moreover, $\varepsilon^q_{n,m} = \Phi^q_{n,m,k} - h^q_{n,m,k}(\hat{\mathbf{s}}_k^-)$ denotes the measurement innovation, and $\mathcal{R}(\cdot)$ is a rounding function to nearest integer. Finally, utilizing (10), while assuming initial integer ambiguity estimate at $k=1$ as $\hat{Z}^q_{m,n,1}$, the unwrapped measurements with cycle control are expressed as $\hat{\Phi}^q_{n,m,k} = \hat{Z}^q_{m,n,1}\lambda_q + \mathfrak{U}(\phi^q_{n,m,k}) + \hat{\Psi}^q_{m,n,k}\lambda_q$.

C. EKF-based Measurement Update with Cycle Control

For notational convenience, the measurement function in (4) and the unwrapped measurements with cycle control from Section III-B, are concatenated over all UE antennas and BSs as $\mathbf{h}_q(\mathbf{s}_k) = [h^q_{1,1}(\mathbf{s}_k), h^q_{2,1}(\mathbf{s}_k), \ldots, h^q_{N,M}(\mathbf{s}_k)]$ and $\hat{\mathbf{\Phi}}^q_k = [\hat{\Phi}^q_{1,1,k}, \hat{\Phi}^q_{2,1,k}, \ldots, \hat{\Phi}^q_{N,M,k}]$, respectively. As a result, by following (3), the measurement covariance for the concatenated measurements reads $\mathbf{\Sigma} = \sigma^2\mathbf{I}_{MN} \in \mathbb{R}^{MN\times MN}$.

Utilizing measurements from the q^{th} frequency band, the a-posteriori estimates of the mean and the covariance can be obtained by the EKF update as

$$\begin{aligned}\hat{\mathbf{s}}_k^+ &= \hat{\mathbf{s}}_k^- + \mathbf{K}_k(\hat{\mathbf{\Phi}}^q_k - \mathbf{h}_q(\hat{\mathbf{s}}_k^-)) \\ \hat{\mathbf{P}}_k^+ &= (\mathbf{I}_{14} - \mathbf{K}_k\mathbf{H}_k)\hat{\mathbf{P}}_k^-,\end{aligned} \tag{11}$$

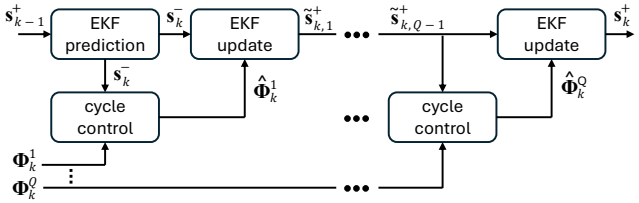

Fig. 2. Illustration of the proposed consecutive measurement update process.

where $\mathbf{K}_k = \hat{\mathbf{P}}_k^-\mathbf{H}_k^T(\mathbf{H}_k\hat{\mathbf{P}}_k^-\mathbf{H}_k^T + \mathbf{\Sigma})^{-1}$ is the Kalman gain. Furthermore, $\mathbf{H}_k \in \mathbb{R}^{MN\times 14}$ is the Jacobian matrix for attaining a linear approximation of the non-linear measurement function. Based on the measurement function (4), the non-zero partial derivatives for $\mathbf{H}_k$ are given as

$$\begin{aligned}\frac{\partial h^q_{n,m}(\mathbf{s})}{\partial \boldsymbol{\theta}} &= \frac{\mathbf{\Gamma}_n^T(\boldsymbol{\theta})(\mathbf{p}_{\text{UE}} + \mathbf{R}(\boldsymbol{\theta})\boldsymbol{\rho}_n - \mathbf{p}_{\text{BS},m})}{\|\mathbf{p}_{\text{UE}} + \mathbf{R}(\boldsymbol{\theta})\boldsymbol{\rho}_n - \mathbf{p}_{\text{BS},m}\|} \\ \frac{\partial h^q_{n,m}(\mathbf{s})}{\partial \mathbf{p}_{\text{UE}}} &= \frac{\mathbf{p}_{\text{UE}} + \mathbf{R}(\boldsymbol{\theta})\boldsymbol{\rho}_n - \mathbf{p}_{\text{BS},m}}{\|\mathbf{p}_{\text{UE}} + \mathbf{R}(\boldsymbol{\theta})\boldsymbol{\rho}_n - \mathbf{p}_{\text{BS},m}\|}, \\ \frac{\partial h^q_{n,m}(\mathbf{s})}{\partial \delta} &= c, \text{ where}\end{aligned} \tag{12}$$

$$\mathbf{\Gamma}_n(\boldsymbol{\theta}) = \left[\frac{\partial \mathbf{R}(\boldsymbol{\theta})}{\partial\alpha}\boldsymbol{\rho}_n \quad \frac{\partial \mathbf{R}(\boldsymbol{\theta})}{\partial\beta}\boldsymbol{\rho}_n \quad \frac{\partial \mathbf{R}(\boldsymbol{\theta})}{\partial\gamma}\boldsymbol{\rho}_n\right]. \tag{13}$$

The detailed formulations for the partial derivatives of $\mathbf{R}(\boldsymbol{\theta})$ with respect to α, β and γ in (13) can be found in [5].

D. Utilization of Multi-Frequency Measurements

Traditionally the EKF update considers all measurements jointly, thus feeding all multi-frequency measurements $[\hat{\mathbf{\Phi}}_k^{1\,T}, \cdots, \hat{\mathbf{\Phi}}_k^{Q\,T}]^T$ into the update step in (11) simultaneously. In the following, we refer to this as a *joint* EKF update. Since the update stage is sensitive to state prediction accuracy through measurement model linearization as well as cycle slips in measurement unwrapping, large UE state dynamics can confuse the EKF update and lead to filter divergence in the worst case.

To diminish the effect of integer ambiguity issues with high carrier frequencies, we propose updating the EKF consecutively per carrier frequency such that the updated UE state using a lower carrier frequency $q-1$, denoted as $\tilde{\mathbf{s}}^+_{k,q-1}$, is used as the input to the update with a higher carrier frequency q. By this way, the improved UE state estimate using a low carrier frequency assist in cycle control of higher carrier frequencies. In the following, we refer to this as a *consecutive* EKF update. Compared to the joint update, the benefit of consecutive update is the improved tolerance against integer ambiguity problem in high mobility scenarios. The consecutive measurement update process is visually illustrated in Fig. 2.

E. Particle Filter Solution for Improved Integer Ambiguity Tolerance in High Mobility Scenarios

Whereas the EKF is limited to a single a-posteriori state estimate $\hat{\mathbf{s}}_k^+$, particle filter represents the a-posteriori state estimate with a set of particles $\{\mathbf{s}_k^{(j)}, w_k^{(j)}\}_{j=1}^{N_{\text{P}}}$, inherently enabling tracking with arbitrary-shaped probability distributions. With large and dynamic state vector, it is often challenging

Algorithm 1 Particle filter processing at time step k

Input: Particle-wise states from previous time step (mean $\mathbf{s}_{k-1}^{(j)}$ and covariance $\mathbf{P}_{k-1}^{(j)}$) and particle weights $w_k^{(j)}$ for $j = 1, \cdots, N_\mathrm{p}$

for $j = 1, \ldots, N_\mathrm{p}$ **do**
  Perform EKF prediction for j^{th} particle according to (9)
  Perform EKF update for j^{th} particle according to (11)
  Sample from a posteriori distibution by EKF update in (11)
  Update weights using (14), and normalize to ensure $\Sigma_j w_j = 1$
end for
if $1/\Sigma_j w_j^2 < N_\mathrm{th}$ **then**
  Resample with replacement
end if

Output: Updated particle-wise states (mean $\mathbf{s}_k^{(j)}$ and covariance $\mathbf{P}_k^{(j)}$) and particle weights $w_k^{(j)}$ for $j = 1, \cdots, N_\mathrm{p}$

to find a good proposal distribution for particle sampling. Therefore, in this paper, we utilize EKF-based particle filter [14], which performs particle-wise EKF prediction and update phases to find a suitable importance density. After each sampling round, the particle weights can be updated as

$$w_k^{(j)} \propto w_{k-1}^{(j)} \frac{p(\hat{\Phi}_{n,m,k}^q | \mathbf{s}_k^{(j)}) p(\mathbf{s}_k^{(j)} | \mathbf{s}_{k-1}^{(j)})}{\pi(\mathbf{s}_k^{(j)} | \mathbf{s}_{k-1}^{(j)}, \hat{\Phi}_{n,m,k}^q)}, \tag{14}$$

where $p(\hat{\Phi}_{n,m,k}^q | \mathbf{s}_k^{(j)})$ is the measurement likelihood density, $p(\mathbf{s}_k^{(j)} | \mathbf{s}_{k-1}^{(j)})$ is the prior density, and $\pi(\mathbf{s}_k^{(j)} | \mathbf{s}_{k-1}^{(j)}, \hat{\Phi}_{n,m,k}^q)$ is the proposal density. If particle efficiency $1/\Sigma_j w_j^2$ drops below a given efficiency threshold N_th, particles are resampled (we define $N_\mathrm{th} = N_p/2$). The involved steps of the utilized particle filtering approach are summarized in Algorithm 1.

Due to approximative nature of particle filters, the tracking accuracy of a particle filter cannot often be improved compared to EKF under mildly nonlinear measurement models. However, when considering high mobility scenarios with challenging integer ambiguity resolution, the utilized particle filter approach enables tracking of multiple parallel EKF branches from which only the most probable ones survive over time. As such, the tolerance against cycle slips can be improved, but at the cost of higher computational complexity proportional to the number of employed particles.

IV. Numerical Results

In this section, we provide the numerical results, focusing on the accuracy of UE positioning and orientation estimation as well as clock synchronization achieved by the proposed carrier-phase-based tracking methods. We consider an example UE track of $60\,\mathrm{s}$ duration with varying 3D position and 3D orientation along with UE clock drifting. The UE is equipped with $N = 6$ antennas placed at corner points of a cube (excluding two opposite corners) with a side length of $5\,\mathrm{cm}$ and centered at the UE position. Furthermore, around the UE track, $M = 4$ base stations are located at coordinates $[0, -6, 3.5]^T$, $[-8, 7, 3]^T$, $[7, 6, 2.5]^T$ and $[-1, 2, 7]^T$. The drifting UE clock is parametrized with a clock skew $\sigma_\xi^2 = 10^{-10}$, which results in clock-originated range drifting of tens of meters during the track. To obtain an initial state estimate, we perform a brute force grid search algorithm. Finally, the standard deviation of measurement noise σ is determined as $1\,\%$ of the wavelength, and the simulations are performed over 100 random trials.

TABLE I
Average EKF tracking errors

Average error	$\Delta t = 20$ ms			$\Delta t = 60$ ms		
[mm] / [deg] / [ps]	pos.	orient.	clock	pos.	orient.	clock
Single frequency						
3.5 GHz	0.57	0.20	0.88	0.61	0.26	1.01
15 GHz	0.14	0.06	0.24	fail	fail	fail
28 GHz	0.08	0.03	0.16	fail	fail	fail
Multi-frequency with *consecutive* update						
3.5&15 GHz	0.14	0.05	0.24	0.25	0.06	0.39
3.5&28 GHz	0.08	0.03	0.16	0.22	0.04	0.34
3.5&15&28 GHz	0.07	0.03	0.15	0.22	0.03	0.34
Multi-frequency with *joint* update						
3.5&15 GHz	0.14	0.05	0.24	fail	fail	fail
3.5&28 GHz	0.08	0.03	0.16	fail	fail	fail
3.5&15&28 GHz	0.07	0.03	0.15	fail	fail	fail

At first, we study the EKF tracking performance over different carrier frequencies, reflecting potential Frequency Range (FR)1, FR2 and FR3 carriers, while assuming two separate measurement update intervals $\Delta t = 20\,\mathrm{ms}$ and $\Delta t = 60\,\mathrm{ms}$. To this end, in Table I, the average EKF tracking errors for the UE 3D position (mm), 3D orientation (deg), and clock (ps) are presented for different frequency combinations and for both the traditional *joint* EKF update method as well as the proposed *consecutive* update method. The results show that with the smaller update interval of $20\,\mathrm{ms}$ the higher carrier frequencies enable smaller estimation errors, thus indicating that the integer ambiguity can be sufficiently resolved. However, when increasing the update interval to $60\,\mathrm{ms}$, tracking with higher frequencies lead to unstable filter operation and eventually cause tracking failures, denoted as 'fail' in Table I. Such tracking failures occur because the measurement interval becomes too large with respect to the wavelength, resulting in inaccurate UE state prediction and eventually causing filter divergence after multiple successive cycle slips. With multi-frequency measurements, similar trend can be seen for the traditional joint EKF update, where using high frequencies clearly limit the performance at the higher measurement interval. However, the proposed consecutive EKF update method is able to operate over all aggregated frequencies and both measurement intervals, while clearly improving the performance compared to single frequency measurements.

To investigate the effect of measurement update interval Δt on the tracking performance in more detail, Fig. 3 presents the average positioning error of EKF-based tracking as a function of the measurement update interval. For all EKF tracking approaches, the positioning error increases gradually in proportion to the measurement update interval, until the performance collapses, as the update interval becomes intolerable and filters diverge. As a reference, to prove the usability of the proposed cycle control method, proposed in Section III-B, also the performance without using the cycle control method is shown to fail already below $10\,\mathrm{ms}$ update interval. Regarding

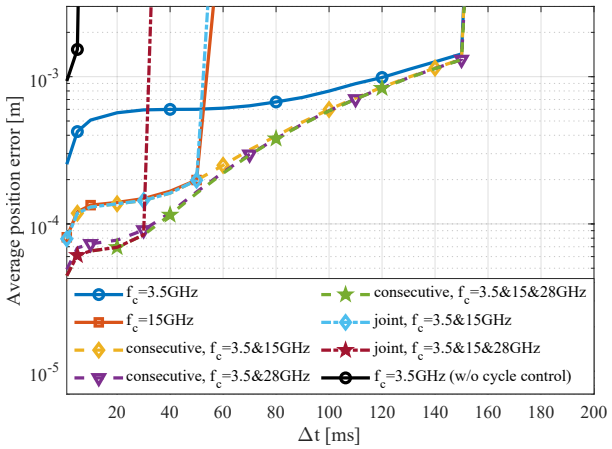

Fig. 3. Average positioning error for EKF tracking as a function of measurement interval Δt, consdering multiple frequency combination options.

multi-frequency measurements, joint and consecutive update approaches reach similar positioning accuracy with small measurement update intervals, but the proposed consecutive update approach is able to operate without failures up to 150 ms whereas the joint update approach collapses below 50 ms.

To further extend tolerable measurement update intervals and simultaneously support high mobility scenarios, we utilize the particle filter presented in Section III-E. To this end, Table II shows the positioning performance for the proposed particle filter using 10, 100 or 1000 particles, including also the EKF approach as a reference. It is noted that the computational complexity of the particle filter increases in proportion to the number of used particles N_p. Furthermore, the performance is evaluated for a single frequency scenario at 3.5 GHz carrier and a carrier-aggregated scenario with 3.5 GHz, 15 GHz and 28 GHz carriers using consecutive measurement update while considering measurement update intervals up to 200 ms. First, the Table II shows tracking availability, which indicates the percent of the random realizations that were successfully carried out without filter divergence. After this, the average positioning errors are shown only for successful realizations (i.e., not over all realizations as in Fig. 3). When considering large measurement intervals with sufficient number of employed particles (N_p $\geq$100), the results indicate that the proposed particle filter can considerably improve the tracking availability compared to the EKF. However, when filtering operates correctly without diverging, the EKF shows the best positioning accuracy, as the particle filter is limited to approximative estimation through particle distributions. In the multi-frequency scenario the proposed particle filter with N_p=100 and N_p=1000 reaches 100 % availability up to 200 ms measurement interval.

TABLE II
PARTICLE FILTER PERFORMANCE IN TERMS OF TRACKING AVAILABILITY AND AVERAGE POSITIONING ERROR

	3.5 GHz			3.5&15&28 GHz		
Δt [ms]	120	160	200	120	160	200
Availability [%]						
EKF	100	56	0	100	75	0
Particle $N_p = 10$	100	94	0	31	0	0
Particle $N_p = 100$	100	100	13	100	100	100
Particle $N_p = 1000$	100	100	81	100	100	100
Average positioning error without failures [mm]						
EKF	0.99	1.58	-	0.84	1.48	-
Particle $N_p = 10$	1.07	1.64	-	0.84	-	-
Particle $N_p = 100$	1.03	1.63	3.10	0.84	1.48	2.32
Particle $N_p = 1000$	1.03	1.62	3.90	0.84	1.48	2.32

V. CONCLUSIONS

In this paper, we studied carrier phase-based tracking of 3D position and 3D orientation of a UE equipped with multiple antennas. Based on EKF framework, we proposed a cycle control mechanism and a specific consecutive measurement update scheme to improve tolerance against integer ambiguity errors. In addition, to further extend the tracking capability to large measurement intervals and high mobility scenarios, we presented a complementary particle filter solution, utilizing the above-discussed EKF framework. The numerical results indicate that the proposed EKF with cycle control provides a good accuracy for relatively large measurement update intervals, extending multiple wavelengths in range. Moreover, particle filters can help in further increasing the update interval and avoiding filter divergence due to cycle slips. In all considered scenarios, the proposed tracking approaches reach sub-degree orientation estimation accuracy and sub-centimeter positioning accuracy, thus indicating promising aspects for future development.

REFERENCES

[1] 3GPP, TR 38.859 V18.1.0, "Study on expanded and improved NR positioning (Release 18)," Jun. 2024. [Online]. Available: www.3gpp.org

[2] 3GPP, TS 22.261 V20.1.0, "Service requirements for the 5G system (Release 20)," Dec. 2024. [Online]. Available: www.3gpp.org

[3] H. Wymeersch, R. Amiri, and G. Seco-Granados, "Fundamental performance bounds for carrier phase positioning in cellular networks," in *Proc. IEEE GLOBECOM*, 2023, pp. 7478–7483.

[4] A. Clemm, *et al.*, "Toward truly immersive holographic-type communication: Challenges and solutions," *IEEE Commun. Mag.*, vol. 58, no. 1, pp. 93–99, 2020.

[5] J. Talvitie, M. Säily, and M. Valkama, "Orientation and location tracking of XR devices: 5G carrier phase-based methods," *IEEE J. Sel. Topics in Signal Process.*, vol. 17, no. 5, pp. 919–934, 2023.

[6] L. Chen, *et al.*, "Carrier phase ranging for indoor positioning with 5G NR signals," *IEEE Internet of Things J.*, vol. 9, no. 13, 2022.

[7] A. Fouda, R. Keating, and H.-S. Cha, "Toward cm-level accuracy: Carrier phase positioning for IIoT in 5G-Advanced NR networks," in *Proc. IEEE PIMRC*, 2022, pp. 782–787.

[8] S. Fan, Y. Ji, and H. Tian, "Triple-frequency carrier phase positioning with optimized ambiguity resolution in 5G New Radio networks," in *Proc. IEEE GLOBECOM 2023*, 2023, pp. 1191–1196.

[9] J. Li, *et al.*, "Carrier phase positioning using 5G NR signals based on OFDM system," in *Proc. IEEE VTC2022-Fall*, 2022, pp. 1–5.

[10] M. Koivisto *et al.*, "Joint device positioning and clock synchronization in 5G ultra-dense networks," *IEEE Trans. Wireless Commun.*, vol. 16, no. 5, pp. 2866–2881, 2017.

[11] S. Fan *et al.*, "Carrier phase-based synchronization and high-accuracy positioning in 5G New Radio cellular networks," *IEEE Trans. Commun.*, vol. 70, no. 1, pp. 564–577, 2022.

[12] 3GPP, TR 38.901 V17.0.0, "Study on channel model for frequency spectrum from 0.5 to 100 GHz (Release 17)," Mar. 2022.

[13] T. K. Y. Bar-Shalom, X. Rong Li, *Estimation with Applications to Tracking and Navigation: Theory, Algorithms and Software*. Wiley Interscience, 2001.

[14] N. Zeng, *et al.*, "Identification of nonlinear lateral flow immunoassay state-space models via particle filter approach," *IEEE Trans. Nanotechnol.*, vol. 11, no. 2, pp. 321–327, 2012.